ELSEVIER

Contents lists available at ScienceDirect

International Journal of Heat and Mass Transfer

journal homepage: www.elsevier.com/locate/ijhmt





Dual-tracer laser-induced fluorescence thermometry for understanding bubble growth during nucleate boiling on oriented surfaces

Mahyar Ghazvini ^a, Mazen Hafez ^a, Cristian Pena ^a, Philippe Mandin ^b, Rosalinda Inguanta ^c, Myeongsub Kim ^a, ^{*}

- ^a Ocean and Mechanical Engineering, Florida Atlantic University, 777 Glades Rd., Boca Raton, FL 33431, US
- ^b Institut de Recherche Dupuy de Lôme, UMR CNRS 6027, Lorient 56100, France
- ^c Dipartimento di Ingegneria, Università degli Studi di Palermo, Viale delle Scienze, Palermo 90128, Italy

ARTICLE INFO

Keywords: Thermal management Nucleate boiling Laser-induced thermometry Temperature-Sensitive Dyes Oriented Surfaces

ABSTRACT

Nucleate boiling is perhaps one of the most efficient cooling methodologies due to its large heat flux with a relatively low superheat. Nucleate boiling often occurs on surfaces oriented at different angles; therefore, understanding the behavior of bubble growth on various surface orientations is of importance. Despite significant advancement, numerous questions remain regarding the fundamentals of bubble growth mechanisms on oriented surfaces, a major source of enhanced heat dissipation. This work aims to accurately measure three-dimensional (3D), space- and time-resolved, local liquid temperature distributions surrounding a growing bubble on oriented surfaces that quantify the heat transfer from the superheated liquid layer during bubble growth. The dual tracer laser-induced fluorescence thermometry technique combined with high-speed imaging captures transient 2D temperature distributions within a 0.3 °C accuracy at a 30 μ m resolution. The results show that the temperature close to the heated surface and bubble interface exhibits an acute transient behavior at the time of bubble departure, and the growing bubble works as a pump to remove heat from the surface with a temperature difference of up to 10 °C during its growth and departure. The experimental results are compared with data available in the literature to validate the accuracy of the technique. It was found that the heat transfer coefficient close to the bubble interface and heater is approximately 1.3 times higher than the heat transfer coefficient in the bulk liquid.

1. Introduction

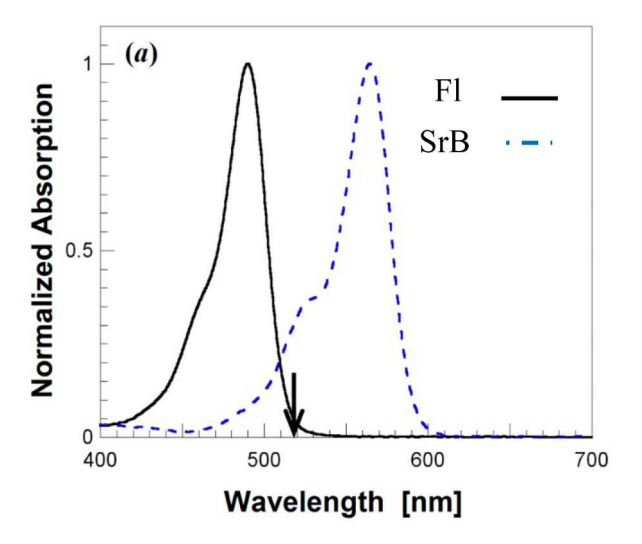
In various engineering applications, nucleate boiling often occurs on surfaces oriented at different angles; therefore, understanding the behavior of bubble growth on various surface orientations is of importance. Numerous studies have highlighted the influence of the orientation of a heated surface on nucleate boiling heat transfer. Storr [1] observed that the heat transfer rate for a given wall superheat increased when rotating the heated surface from horizontal to vertical. Marcus and Dropkin [2] and Githnji and Sabersky [3] have found that the heat transfer coefficient increases from an inclination angle of 0° to 90° According to Marcus and Dropkin, the observed phenomenon can be attributed to the enhanced turbulence of the superheated boundary layer created due to the elongated path followed by the departing bubbles along the surface, which is a result of the increased surface angle.

Further research indicated that the heat transfer coefficient con-

tinues to increase up to an angle between 150° and 170° and then decreases dramatically as the angle approaches 180° [4-7]. Nishikama et al. [7] performed experiments to understand the effect of surface configuration on nucleate boiling heat transfer of a copper flat plate whose orientation was varied from 0° to 175° from the horizontal plane. They concluded that the heat transfer coefficient increases at low-heat flux due to removal of the superheated liquid layer by sweeping bubble slug (merged bubbles) and independency of heat transfer coefficient on orientation at high-heat flux. Rainey and You [1] investigated the effect of heater size and surface orientation on pool boiling heat transfer. They concluded that the heat transfer performance showed a dramatic decrease when increasing the angle of surface orientation from 90° to 180° For the downward-facing inclination ($\theta > 90^{\circ}$), the departing bubbles tended to flatten against the surface and merge with neighboring bubbles. These bubbles also exhibited a noticeably reduced rise velocity. This flattened and reduced rise velocity caused an increase in the residence time of the vapor bubbles, as well as vapor quality, which

E-mail address: kimm@fau.edu (M. Kim).

^{*} Corresponding author.



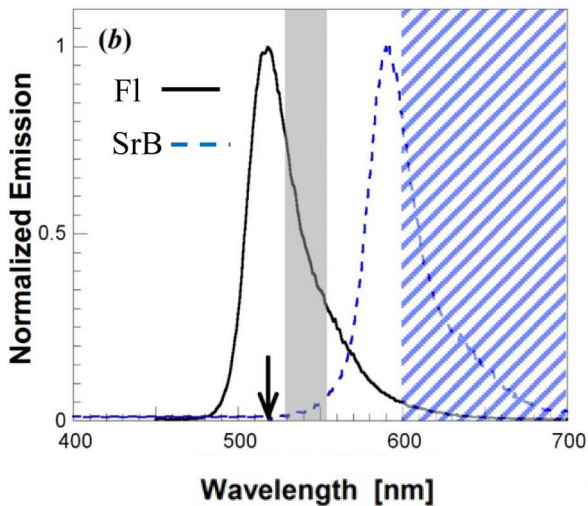


Fig. 1. Absorption (left) and emission (right) spectra for Fl (solid line) and SrB (dashed line). The arrows on both spectra indicate the excitation at 514 nm; the shaded and hatched regions on the emission spectrum denote the wavelengths transmitted by the filters that isolate the emissions from Fl and SrB, respectively [8].

increases the resistance to heat transfer. Also, El-Genk and Suszko [5] performed experiments to determine the effect of inclination angle and liquid subcooling on nucleate boiling on copper surfaces. They concluded that at low heat fluxes (<5 W/cm²) in the discrete bubble region, h_{NB} (a nucleate boiling heat transfer coefficient) increased with higher surface inclination angles. This was attributed to the induced mixing caused by sliding bubbles in the boundary layer along the heated surface. However, in the fully developed and bubble's coalescence regions at intermediate and high applied heat fluxes, h_{NB} decreased with increasing surface inclination. In these boiling regions, the accumulation and coalescence of vapor bubbles introduced a resistance to heat removal from the surface. Consequently, the surface temperature increased, leading to a decrease in h_{NB} as the surface inclination angle increased. They reported that the values of h_{NB} at the surface inclinations of 90° (vertical), 120°, 150°, and 180° (downward facing), are respectively 91 %, 80 %, 62 % and 36 % of the values in the upward facing orientation (0°).

Although the literature has highlighted the impact of surface orientation on nucleate boiling heat transfer, previous studies have predominantly examined the effect of surface orientation on the heat transfer coefficient when multiple bubbles are present on a surface, with limited focus on the isolated bubble behavior with an artificial nucleation site. In this work, we aim to fill this research gap by investigating the impact of different surface orientations, including the horizontal position (0°) as well as inclinations of 30°, 60°, and 90° (Fig. 7a), on a transient heat transfer near a growing bubble in the presence of an artificial nucleation site using dual-tracer fluorescence thermometry (DFT). DFT offers non-invasive, transient liquid temperature measurements at a microscale [8]. The reported accuracy of DFT for temperature measurements is as small as 0.17 $^{\circ}\text{C}$ as it removes the effect of the excitation intensity (input laser light) on the measurements [9]. For a given fluorophore solution at a known molar concentration C, its emission intensity (I_f) is expressed [10]

$$I_f(T) = AI_0g(T) \tag{1}$$

where A is the collection efficiency of the imaging system, I_0 is the intensity of the excitation (i.e., illumination), and g(T) depends on the quantum yield and the molar absorption coefficient of the fluorophore [11]. The temperature (T) can be obtained from the relationship between I_f and T.

DFT employs a ratiometric approach that decouples the variations in laser intensity to improve a measurement accuracy—The ratio of the emissions from two different fluorophores, A and B, excited by the same

illumination $(I_0^A = I_0^B)$ is expressed [12]

$$I'(T) = \frac{I_f^A(T)}{I_f^B(T)} \frac{g_A(T)}{g_B(T)}$$
 (2)

Coppeta and Rogers [13] were the first to describe a ratiometric scheme and presented a comprehensive analysis of various temperature-sensitive fluorophores. They demonstrated that the ratio of signals obtained from fluorescein (Fl) and rhodamine B (RhB) enabled the accurate determination of two-dimensional mean steady-state temperature fields within a thermal plume, achieving a precision of 1.8 °C. Sakakibara and Adrian [9] employed the DFT from RhB and rhodamine 110 (Rh110) to measure water temperature, achieving an accuracy of 0.17 °C.

Recently, studies on boiling phenomena using the DFT technique have helped researchers better understand heat transfer mechanisms involved in boiling. Tange et al. [14] investigated the temperature distribution around multiple boiling bubbles generated in a confined space with DFT. Abdelghany et al. [15] used the DFT thermometry to map the local and temporal temperature fields around boiling bubbles and above the heat-transfer surface using RhB and Rh110. They found that the upward movement of the vapor bubble induces the superheated liquid layer to be pulled and stretched, which is consistent with the phenomenon of scavenging of the superheated liquid layer, as reported in the literature [16].

Despite the existence of some pioneering studies on temperature measurements near a growing bubble, there is a significant research gap. While some studies have delved into temperature measurements near growing bubbles [4–7,17,18], the current state of the literature predominantly emphasizes the influence of surface orientation on nucleate boiling heat transfer. Notably, it is important to highlight that most of these studies have primarily focused on scenarios involving multiple bubbles on a given surface. The existing research landscape has placed a substantial emphasis on understanding the heat transfer coefficient in the presence of multiple bubbles, leaving a noticeable void in our understanding of the isolated behavior of a single bubble with an artificial nucleation site under varying surface orientations. Moreover, no previous studies have addressed the measurements of space- and time-resolved two-dimensional (2D) liquid temperature distributions surrounding a growing bubble on oriented surfaces, which enable a quantitative assessment of the heat transfer from the superheated liquid layer to a vapor bubble. In this study, DFT was employed with thin film illumination to measure 2D bulk fluid temperature fields near the growing bubble on different surface orientations within 0.3 °C at a 30

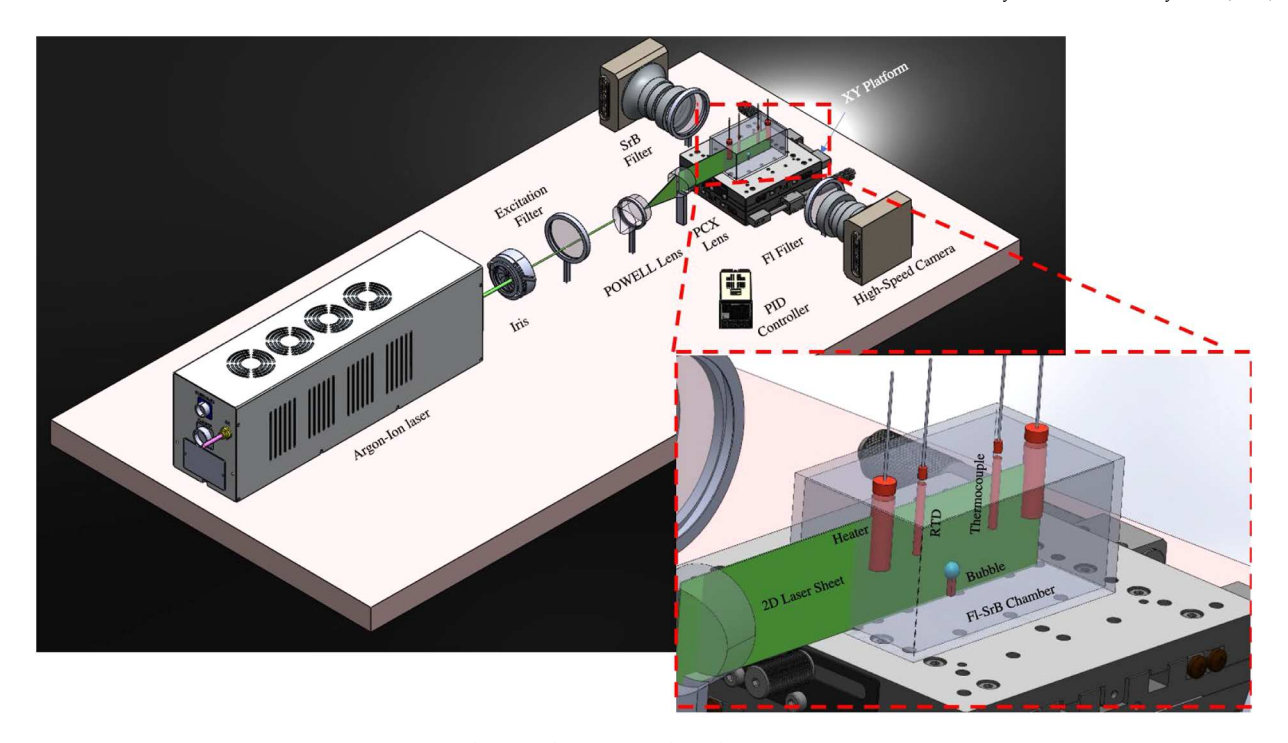


Fig. 2. The optical systems used for the DFT experiments.

 μm resolution. To visualize 3D temperature fields, multiple 2D fields have been measured on different layers near the growing bubble. Our findings reveal that the average liquid temperature around a single bubble increases as the surface orientation changes from 0° to 90°

2. Materials and methods

2.1. Fluorophore solution

The majority of temperature-sensitive fluorophores show an emission intensity that decreases with increasing temperature; this negative correlation is due to the nonradiative dissipation, which, in most cases, increases with temperature [8]. However, fluorescein (Fl) depicts a

positive correlation with an emission intensity that, when excited at a wavelength $\lambda=514$ nm (significantly off its absorption peak), increases with temperature [19]. Sulforhodamine B (SrB) was chosen as the second fluorophore because: (1) it can also be excited at 514 nm due to its relatively broad absorption spectrum; and (2) its emission band, with a peak at 591 nm, has little overlap with that of Fl, with a peak at 518 nm [20].

Fig. 1 shows the normalized absorption spectra (left) and the normalized emission spectra (right) as a function of wavelength at $5\mu mol/L$ Fl (solid line) and $5\mu mol/L$ SrB (dashed line) in the same deionized (DI) water at pH 9.2 [8]. The absorption spectra verify that both Fl and SrB can be excited at a wavelength of 514 nm. The emission spectra show that the fluorescence from the Fl and the SrB can be

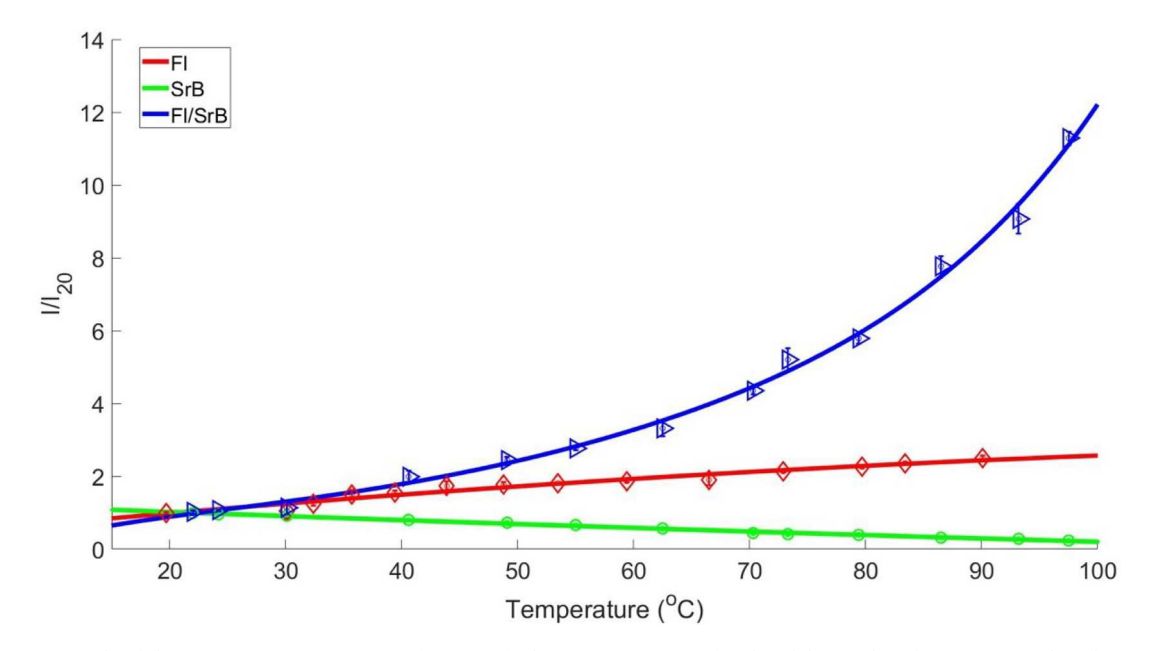


Fig. 3. An average normalized fluorescence intensity I/I_{20} as a function of solution temperature T for Fl (red diamond) and SrB (green circle). The ratio of intensities from Fl and SrB ($I_{\rm Fl}/I_{\rm SrB}$) is shown in blue triangle.

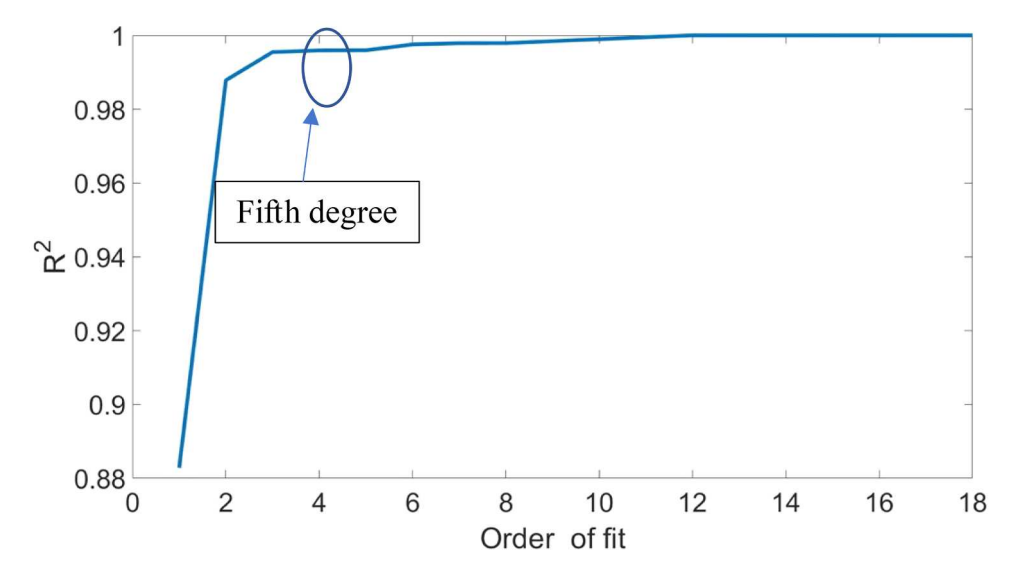


Fig. 4. A relationship between the order of polynomial curve fit and R^2 value for I_{Fl}/I_{SrB} .

isolated from each other using appropriate emission filters–a bandpass filter (525 nm $< \lambda <$ 555 nm, ET540/30 m, Chroma Tech.) and a long pass filter (> 600 nm, 25 mm Dia. Edmound Optics) were used for Fl and SrB, respectively. The effect of FL emissions on SrB emissions (i.e., cross-talk) was no more than 0.1 % of the total signal [20].

2.2. Optical system

To accurately quantify the transient local heat fluxes and 3D mapping of transient fluid temperature at a microscale spatial resolution, a thin microscale laser sheet must be created. A continuous-wave (CW) air-cooled argon-ion laser (Modu-Laser, Stellar-Pro-Select 150) was used to create the laser sheet, which provides multi wavelengths from 457.9 nm to 514.5 nm. The laser beam passed through an iris (10 OD, Edmundptics) to remove higher-order spatial modes and a laser excitation filter (z514/10x, Chroma Tech.) subsequently to isolate the light at λ = 514 nm. The 514 nm beam is then passed through a Powell lens (Edmund Optics), also known as a laser line generator lens, which diverges laser beams and creates a thin 2D laser sheet. Then, it is passed through a PCX cylinder lens (12.5 mm diameter illumination grade, Edmund Optics) to convert laser beams into uniform, straight lines. Then, the optical mirrors are adjusted to ensure that the 2D laser sheet illuminates the appropriate region of interest. The laser light sheet has a thickness of 0.1 mm. Two high-speed cameras (Fastec IL5) with 2x magnification lenses are used from two sides of the boiling chamber to capture emissions of Fl and SrB near the growing bubble. Fig. 2 shows a schematic diagram of the optical system and the 2D laser sheet setup.

2.3. Fluorescence thermometry calibrations

The relationship between fluorophore's emission and temperature was calibrated in the same boiling chamber with the designed optical system at temperatures $T=20-100\,^{\circ}\text{C}$. The temperature of the DI water in the chamber was maintained constant using a PID controller (Platinum high performance PID controller, OMEGA Engineering). Two cartridge heaters and a K-type thermocouple and one RTD were immersed from the top of the solution to control and regulate the liquid temperature (Fig. 2). A sequence of 140 images was acquired for both the Fl and SrB emissions, respectively. After compensating for camera nonlinearities, the grayscale values were spatially averaged over a 38×38 pixels $(0.5\times0.5\text{ mm}^2)$ region in the center of the chamber and then temporally averaged. Fig. 3 shows the average intensity, I, normalized by that at $20\,^{\circ}\text{C}$, I_{20} , as a function of solution temperature T

measured by the thermocouples at T=20-100 °C for Fl (red diamond) and SrB (green circle). The calibration for Fl and SrB were repeated and consistent over five independent experiments. The fluorescence from Fl increases by about 2.44 % per °C, based on a linear curve-fit, whereas the signal from SrB decreases by about 1.54 % per °C. Both temperature sensitivities are in good agreement with the 2.43 % per °C and the 1.55 % per °C, reported by Coppeta and Rogers [19] for Fl and SrB, respectively. The ratio of $I_{\rm Fl}/I_{\rm SrB}$ was fitted to a polynomial function. As the order of the polynomial curve fit increases, the R^2 value may also increase. However, the increase in \mathbb{R}^2 is due to overfitting, where the model fits the noise in the data and the underlying signal, leading to poor generalization to new data. Therefore, the optimal order of polynomial curve fit depends on the balance between capturing the underlying trend in the data and avoiding overfitting. This balance can be achieved by selecting the order of polynomial that results in the highest R^2 value while minimizing the complexity of the model. Thus, in this study, the fifth-order polynomial curve fit for $I_{\rm FI}/I_{\rm SrB}$ was selected (Figs. 4 and 5), as follows.

$$T[^{*}C] = -0.004531 \times \overline{I}^{5} + 0.1176 \times \overline{I}^{4} - 0.9379 \times \overline{I}^{3} + 1.02 \times \overline{I}^{2} + 20.85 \times \overline{I} + 2.512$$
(3)

where T and \bar{I} are temperature and the ratio of average normalized fluorescence intensities ($I_{\rm Fl}/I_{\rm SrB}$), respectively.

2.4. Fin structures

A formation of a large single bubble from a heated surface is key to accurately differentiating temperature distributions by DFT at different planes. For this purpose, we introduced a fin structure with an artificial nucleation site (0.5 mm in diameter), enabling the creation of a single bubble from a heated surface as large as 1.5 mm in length. The nucleation site was artificially fabricated on top of a regular heat sinks by a milling tool. The addition of an artificial nucleation site provides a preferential location for bubble formation, which leads to more uniform and controlled bubble growth [21]. A 3D optical profilometer (Keyence VR-6000) was used to perform non-contact surface and roughness measurements on the fin structure at a resolution of 0.1 μm , as shown in Fig. 6.

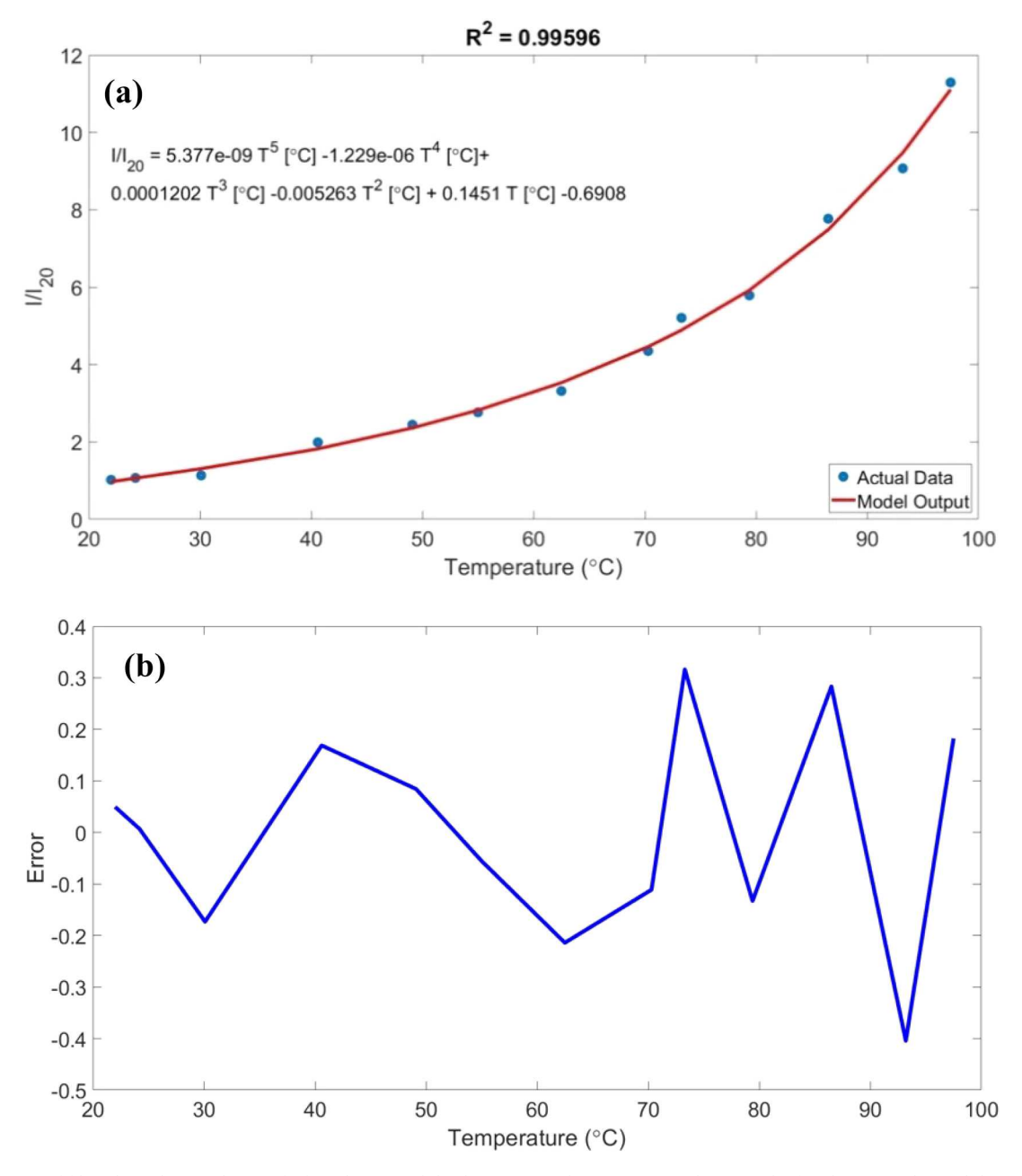


Fig. 5. a) A fifth-order polynomial curve fit for IFI/ISrB with b) the corresponding error (error between the fitted curve and actual data point).

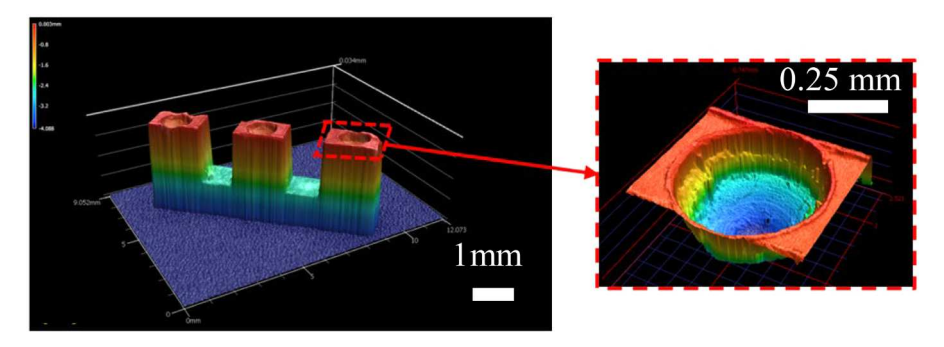


Fig. 6. 3D profiles of three fin structures with artificial nucleation sites.

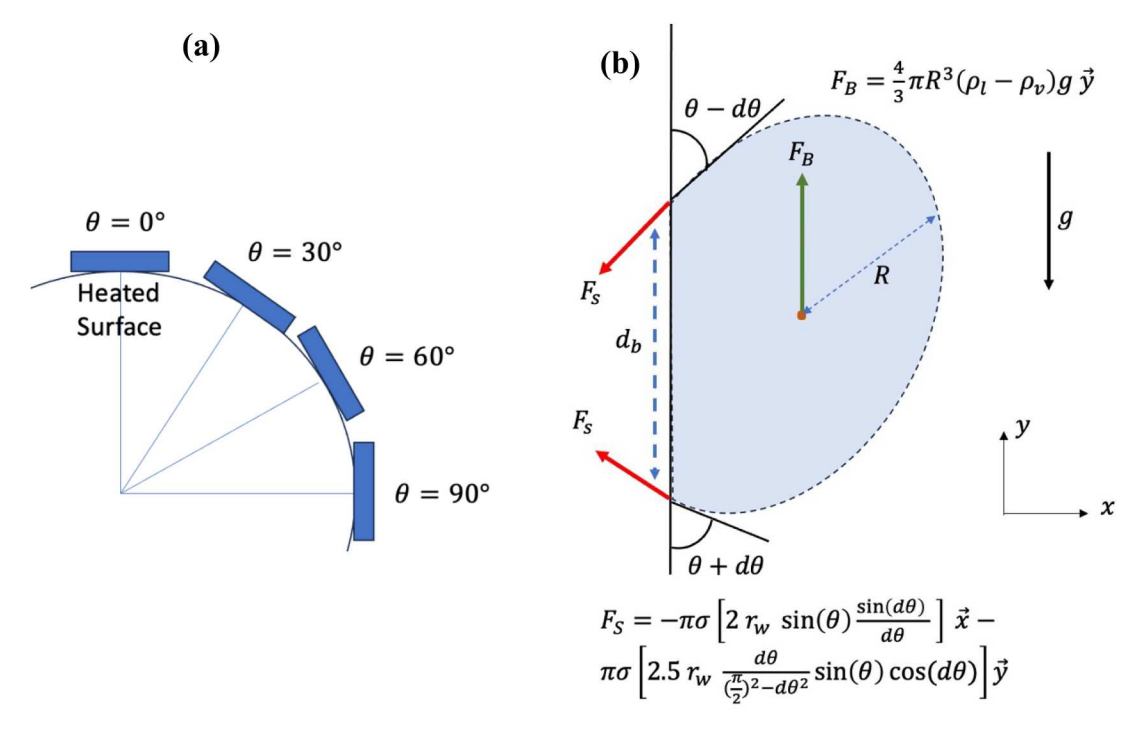


Fig. 7. Schematics of a) the orientation of a heated surface from 0° to 90° and b) forces acting on a bubble on a vertical heater [22].

3. Results and discussion

Time-dependent images of the bubble on different phases from initiation, growth, and departure, at various surface orientations (Fig. 7a) were captured and examined frame by frame to determine bubble dynamics parameters appeared repeatedly at each orientation. Only the images that were most representative of the boiling process are presented in this section. Fig. 7b shows a schematic diagram of forces acting on a bubble on a vertical heater [22]. The buoyancy force results from the weight of the bubble and the integration of the static liquid pressure over its surface. The surface tension force arises from the attractive interaction between the liquid and the surface. The surface tension force acts along the perimeter of the bubble's base and is directly related to the surface tension of the fluid multiplied by the size of the angle formed between the surface and the fluid [22].

3.1. Effect of surface orientation on bubble deformation and bubble dynamics parameters

Fig. 8 shows a series of time-dependent images of a growing bubble during its initiation, growth, and departure on different surface orientations from 0° to 90° Comparing images captured for different orientations, it becomes apparent that the dynamic changes in bubble shape undergo depending on the surface orientation, especially during growth and departure. As the surface inclination increases, bubbles tend to elongate and stretch in the direction of the inclination.

Fig. 9 shows a schematic diagram of a bubble deformation on a surface. The deformation ratio of a bubble (defined as the ratio between the length of the major axis of the bubble to the length of its minor axis = b/a), influenced by surface orientation, is a factor in understanding the bubble dynamic parameters in nucleate boiling [23]. Research has shown that the orientation of a heated surface can cause variations in the deformation ratio during the boiling process [23,24]. Our experimental data show that as the surface orientation increases from 0 to 90°, the deformation ratio of the bubble increases, as shown in Fig. 10a. This indicates that bubbles become more elongated and stretched in the increase of the surface inclination. This phenomenon can be attributed to the interplay between buoyancy and surface tension forces acting on the

bubble (Fig. 10a). When the surface is inclined, the surface tension force acting on the bubble becomes stronger in the vertical direction downward, while the buoyancy force tends to move the bubble upward. As a result, the bubble tends to elongate and deform along the direction of the inclination [22]. The increased deformation ratio with surface orientation indicates a change in the shape of the bubble.

Fig. 10b further highlights the relationship between surface orientation and the bubble base diameter. It shows that increasing the surface orientation results in a larger bubble base diameter due to the buoyancy force acting on the bubble. This change in the base diameter along with the varying surface tension and buoyancy forces in different surface orientations affects the bubble departure diameter and frequency (Fig. 11). As depicted in Fig. 11a, the bubble departure diameter increases when the surface orientation increases from 0° to 90°, and the bubble tends to attach to the surface longer (Fig. 11b). The reason is that due to the bubble deformation, the bubble base diameter is higher at 90° surface compared to 0°, thus, the surface tension which tends to keep the bubble on the surface is higher. This behavior is particularly evident at low heat flux levels when there are no neighboring bubbles merging, and the heated surface area is limited. This is because the fin structure has a limited surface area as the heated surface (2 mm in length). In such cases, the bubble lacks the ability to slide upward along the surface and separates from the surface, as reported in the existing literature [5,6].

3.2. Effects of surface orientation on liquid temperature distribution

The effects of surface orientation on the distribution of liquid temperature around a growing bubble were investigated using DFT. The analysis revealed approximately 14% variations in the liquid temperature distribution between 0° to 90° surface orientation at the same time after initiation. Fig. 12 shows the overall liquid temperature distribution at 8 s after initiation around a growing bubble, which increases from 0° to 90° inclination. For comparison, the average liquid temperature was measured across a 100-pixel by 100-pixel area, (area 1 in Fig. 12, fixed area for all four cases) equivalent to a spatial dimension of 0.5 mm by 0.5 mm, for all surface orientations. At 0° surface orientation, the average liquid temperature was found to be 78.39 °C. As the surface orientation increased to 30°, the average liquid temperature rose to

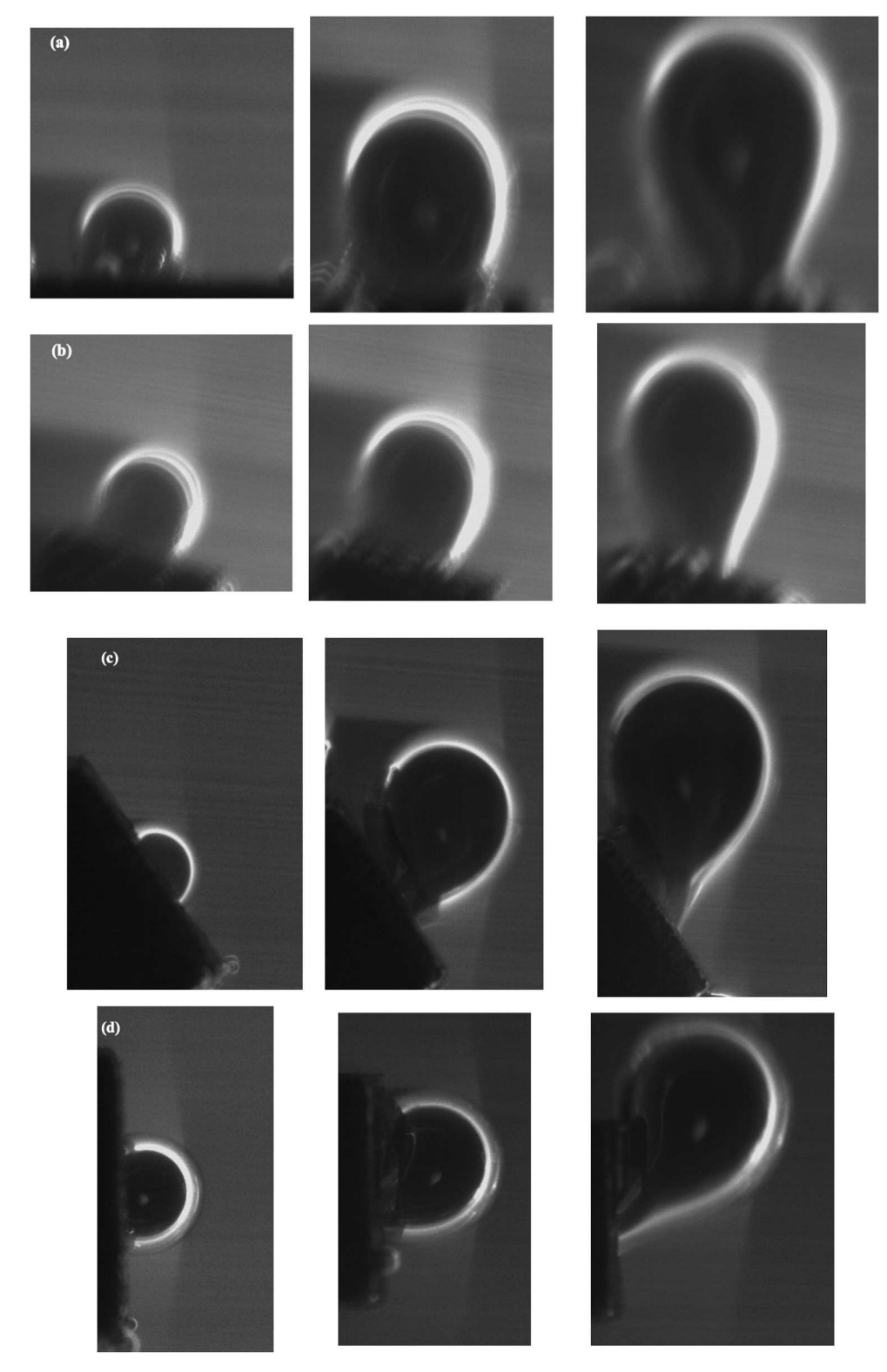


Fig. 8. A series of representative images of a growing bubble during its initiation, growth, and departure at a) 4 s, 10 s, and 28 s after initiation on 0°, b) 4 s, 10 s, and 28 s after initiation on 30°, c) 2 s, 8 s, and 28 s after initiation on 60°, and d) 3 s, 8 s, and 28 s after initiation on 90° oriented surfaces.

 $83.25\,^{\circ}\text{C}$, indicating a notable temperature elevation. Further increasing the surface orientation to 60° resulted in an average liquid temperature of $85.55\,^{\circ}\text{C}$, indicating a continued upward trend. Finally, at a surface orientation of 90° , the average liquid temperature reached its highest value of $88.64\,^{\circ}\text{C}$. These results clearly demonstrate a progressive increase in average liquid temperature as the surface orientation approaches perpendicular (90°) , emphasizing the significance of surface

orientation in influencing the liquid temperature distribution surrounding a single bubble. This phenomenon can be explained by the combined effects of liquid replenishment and the convective heat transfer associated with the bubble motion (bubble departure frequency). At a surface orientation of 0° (horizontal surface), the bubble tends to detach relatively quickly (Fig. 11b). As a result, the liquid surrounding the bubble is exposed to the heated surface for a shorter

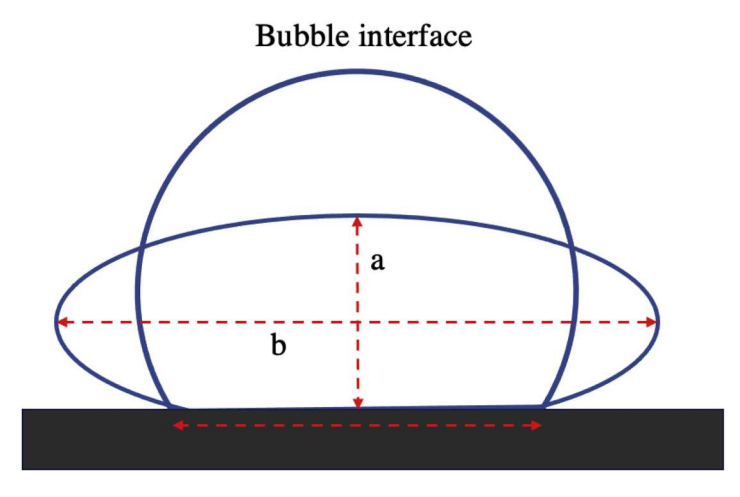
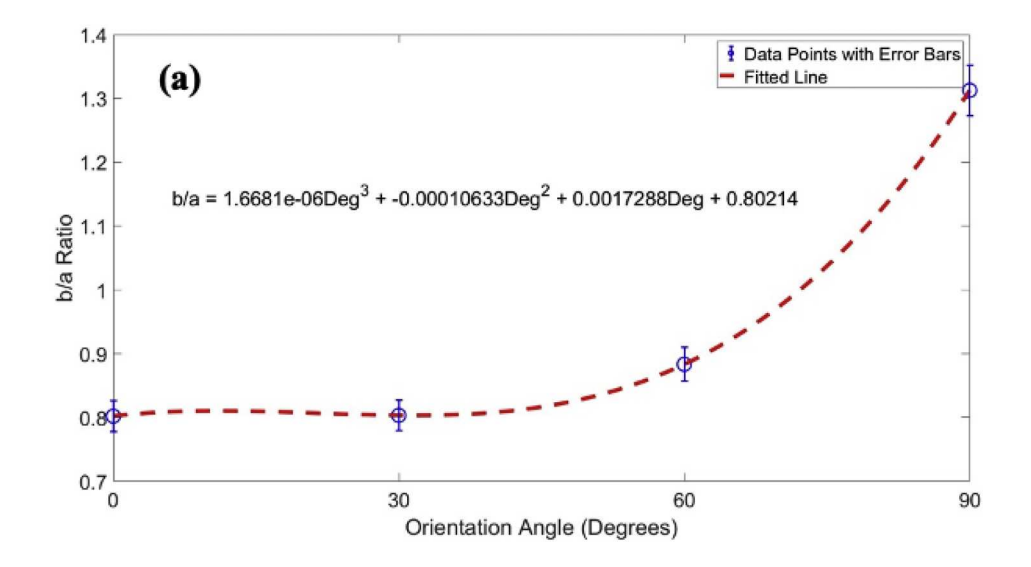
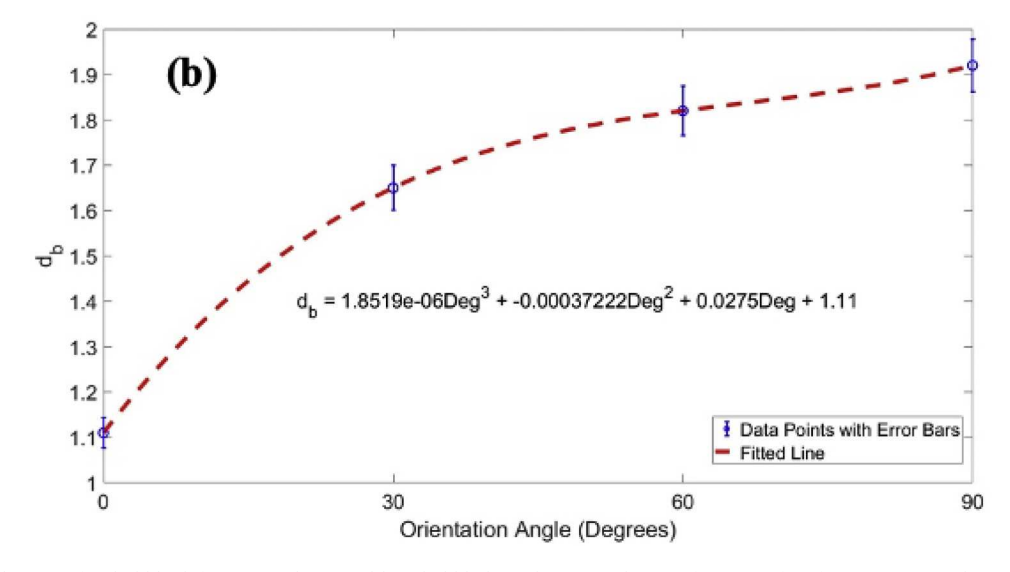


Fig. 9. A schematic of bubble deformation, including a deformation ratio (b/a) and a bubble base diameter (d_b) .





 $\textbf{Fig. 10.} \ \ \text{Changes of a) bubble deformation (b/a), and b) a bubble base diameter (d_b) as a function of surface orientation during its growth. \\$

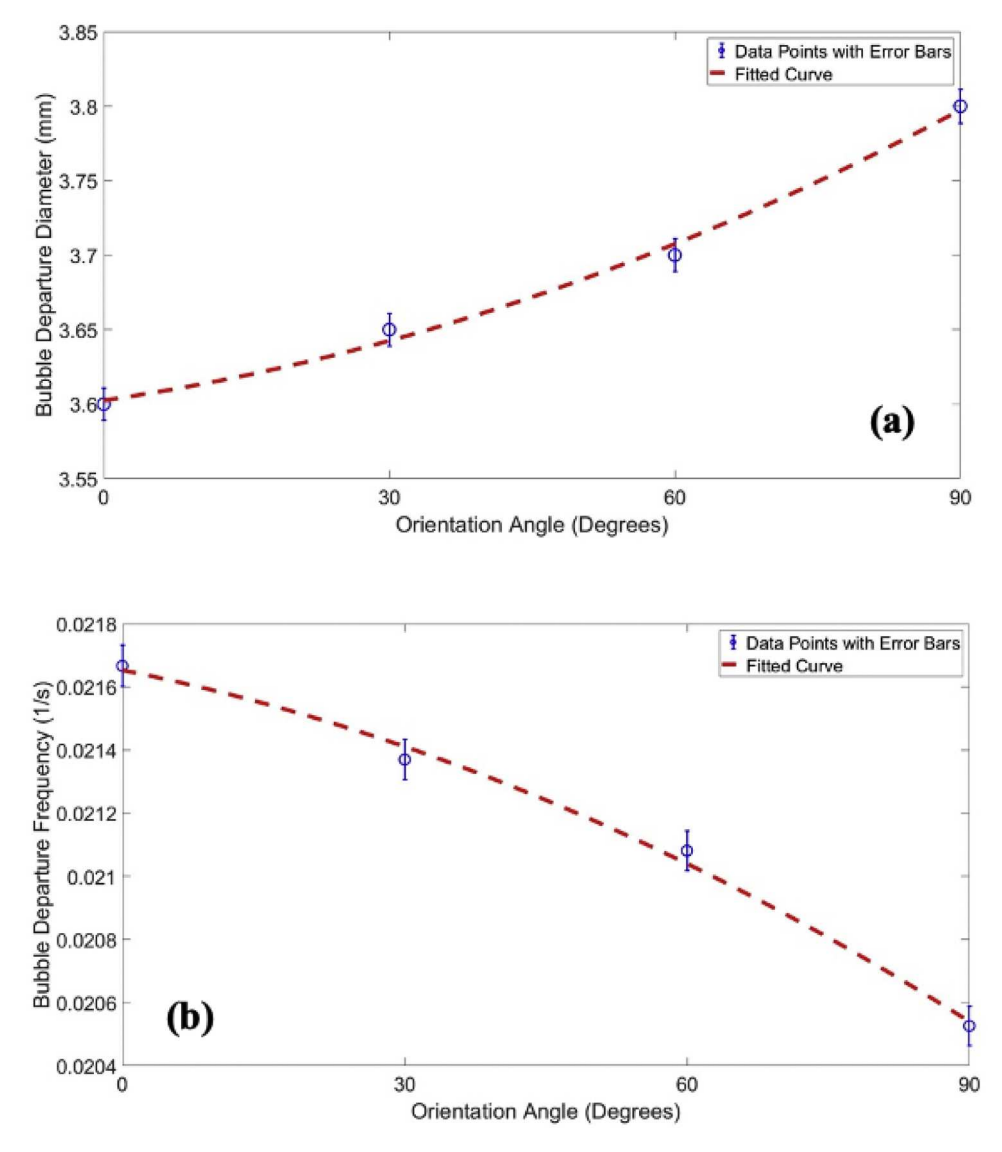


Fig. 11. Changes of a) a bubble departure diameter (d_b) , and b) a bubble departure frequency as a function of surface orientation.

period, limiting the time available for heat transfer. Therefore, the temperature rise in the liquid is relatively smaller compared to higher surface orientations.

3.3. Transient liquid temperature distributions on different surface orientations

This section focuses on the transient liquid temperature around a growing bubble on different surface orientations during its growth and departure time. We aim to investigate the interplay between surface orientation, bubble behavior, and heat transfer characteristics by analyzing the transient liquid temperature profiles. As an example, the bubble expansion and shrinkage lead to liquid temperature change around the bubble, resulting in a variation in the heat transfer coefficient. At given time, three different locations in the fluid are chosen, where the temperature was averaged over a spatial resolution of 10×10 pixels, corresponding to $50~\mu m \times 50~\mu m$.

Fig. 13 illustrates the liquid temperature distribution 8–10s after initiation during the growth stage on a 0° surface, where $T_{saturated} \cdot T_{bulk} \approx 20$ °C, indicating non-uniformity. The bubble diameter is approximately 2.1 mm. This non-uniformity primarily arises from the formation of a superheated liquid layer near the heated surface. While heat transfer within the bubble intensifies as this layer expands, temperature non-

uniformity is most pronounced in the early stages of growth, transitioning to a more uniform distribution later on (Fig. 13a and 13b). Fig. 13a depicts the liquid temperature distribution during the growth phase, coinciding with the formation of the superheated liquid layer (500 μ m). As the growth progresses, the superheated liquid layer expands along the y-axis, eventually covering the entire bubble (Fig. 13b).

Fig. 14a shows a liquid temperature distribution around a growing bubble at 22 s after its initiation right before departure, including three different locations specifically selected to compare transient temperature information. Fig. 14b and 14c show the corresponding transient liquid temperature profiles at these locations and the evolution of the bubble diameter over time, respectively. To capture the temporal evolution of both temperature and diameter, a rigorous analysis such as image capturing, image mapping, pixels' temperature measurements, and bubble diameter measurements was conducted, involving the examination of approximately 750 frames. Fig. 14b shows a sudden jump and drop on temperature between 8 and 12 s, corresponding to expansion and shrinkage of the bubble observed from high-speed imaging. We quantified that the variation of temperature during expansion and shrinkage was in the range of 3.8 %-6.6 % above the average value. Specifically, the expansion of the bubble starts at t = 8 s, resulting in the liquid-vapor interface reaching location 3 with a sudden temperature increase (6.6 % instant temperature rise, $\Delta T = T_9 - T_8 \cong 3.6$ °C).

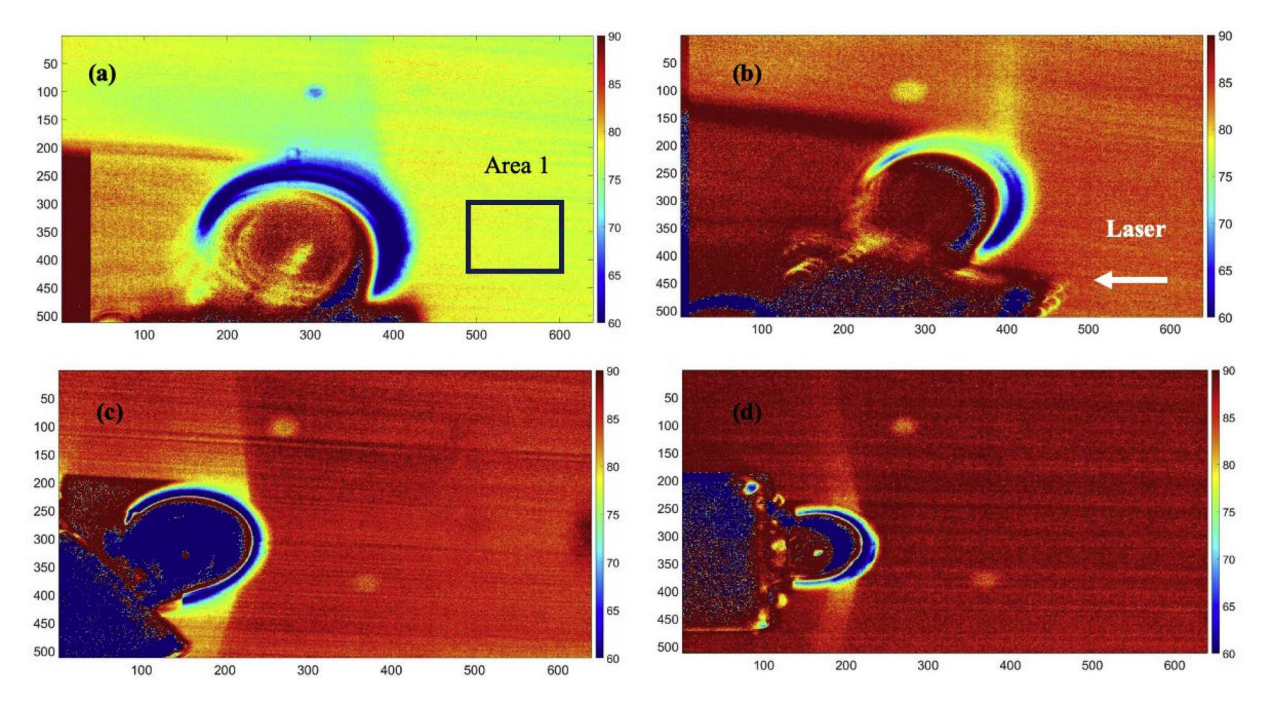


Fig. 12. Liquid temperature distributions around a growing bubble at the same time after initiation on a) 0° b) 30°, c) 60°, d) 90° oriented surfaces.

During the expansion phase, as the bubble grows, it accumulates vapor from the heated liquid. The expansion of the bubble brings hot vapor into close contact with the surrounding bulk liquid (locations 2 and 3). This contact allows for efficient heat transfer from the vapor phase to the liquid phase. As a result, the local liquid temperature in the vicinity of the expanding bubble increases. Also, the liquid temperature near the heated surface (location 1) and within the liquid (location 2) exhibits a similar behavior to that at location 3, albeit with a lesser temperature increase (temperature difference at t=8 s and t=9 s, $\Delta T=T_9-T_8~\cong~1.$ 6°C and $\Delta T = T_9 - T_8 w \cong 2.1$ °C, respectively). On the other hand, at the time of departure, (t=28 s), as the bubble begins to detach from the heated surface, the liquid temperature close to the heated surface and the bubble interface (i.e., location "1") drops 2-3 °C [18]. This temperature drop can also be seen in locations 2 and 3 (2-3 °C). This temperature drop can be attributed to the removal of the thermal boundary layer around the heated surface by the departing bubble and the influx of colder liquid.

Fig. 15 shows a liquid temperature distribution, transient liquid temperature profiles, and a corresponding bubble diameter for the 30° surface orientation. Fig. 15a shows the liquid temperature distribution around a single bubble on 30° surface, in which x and y are pixel values. Fig. 15b shows that the transient temperature profiles of locations 2 $(T \approx 76 - 77^{\circ}\text{C}, 1250 \ \mu\text{m} \text{ approximate distance from the heater)}$ and 3 $(T \approx 75 - 76^{\circ}\text{C}, 2500 \,\mu\text{m} \text{ approximate distance from the heater)}$ are quite similar prior to the departure time (t < 7s). This similarity is attributed to their relative distance from the bubble interface. On the other hand, liquid temperature at location 1 is at 81 °C higher on average and fluctuates more (\sim 2 °C) compared to 75.8 °C and 76.2 °C at the other two locations, respectively. The higher fluctuation at location 1 is attributed to its close proximity to both the heated surface and the bubble interface. Firstly, location 1 is situated near the heated surface. When a surface is heated, it transfers heat to its surroundings through conduction, which is the transfer of heat through direct contact. In this case, the heated surface transfers heat to the surrounding medium, which includes location 1. Due to its proximity, location 1 receives a higher amount of heat from the heated surface compared to other locations, leading to more intense heat transfer effects. Secondly, being in close proximity of location 1 to the bubble interface experiences more significant heat transfer effects. This is because the interface acts as an additional heat source or sink, leading to enhanced fluctuations in temperature at that location. At the time of departure, there is a sudden temperature drop at location 1 ($\Delta T = T_8 - T_7 = -3.7^{\circ}$ C) due to the thermal boundary layer removal. Simultaneously, liquid temperature at location 3 experiences a sudden increase ($\Delta T = T_8 - T_7 = 1.6^{\circ}$ C) at $t = 7 \sim 8$ s as a result of the bubble's upward movement during departure. This upward movement removes the thermal boundary layer from the surface, leading to the temperature increase. Fig. 15c shows the bubble diameter over time, indicating the bubble diameter at the time of departure ($t = 7 \sim 8$ s).

Fig. 16 shows a liquid temperature distribution and its change on a 90° surface orientation. Fig. 16a shows that the highest liquid temperature is more than 95 °C, attached to the heated surface. Fig. 16b shows that the expansion and subsequent shrinkage of the bubble result in a temperature rise of 5.2 % at location 4. This temperature increase occurs due to the bubble's expansion, which causes the liquid-vapor interface to reach location 1. During the departure at approximately $t\approx 8$ s, there is a temperature rise and drop (2.3 % temperature change) at location 4 due to the upward bubble movement at that time (see Fig. 8d) ($\Delta T =$ $T_9 - T_8 = -2^{\circ}$ C). In contrast, locations 1, 2, and 3 experience less than 1 % temperature change during this time. This negligible temperature variation is primarily attributed to the upward movement of the bubble and cold liquid agitation at the time of departure (Fig. 16b). At a 90° surface orientation, the forces acting on the bubble (Fig. 7b) cause more deformation in the bubble shape compared to 0° and 30°. As a result, the liquid-vapor interface becomes closer to location 4 and relatively farther away from locations 1, 2, and 3, resulting in unique temperature variations, as shown in Fig. 16b.

3.4. Temperature profile along x and y

We quantified liquid temperature gradients along different x and y locations during bubble growth as they provide a quantitative measure of heat transfer from liquid to the vapor bubble. The Gaussian smoothing algorithm was used to smooth out noise in temperature signals. The temperature data underwent smoothing with an index of 5, resulting in a maximum smoothing effect of approximately 0.2–0.3 $^{\circ}$ C in the measurements.

Fig. 17 shows the liquid temperature distribution at t = 8 s after the

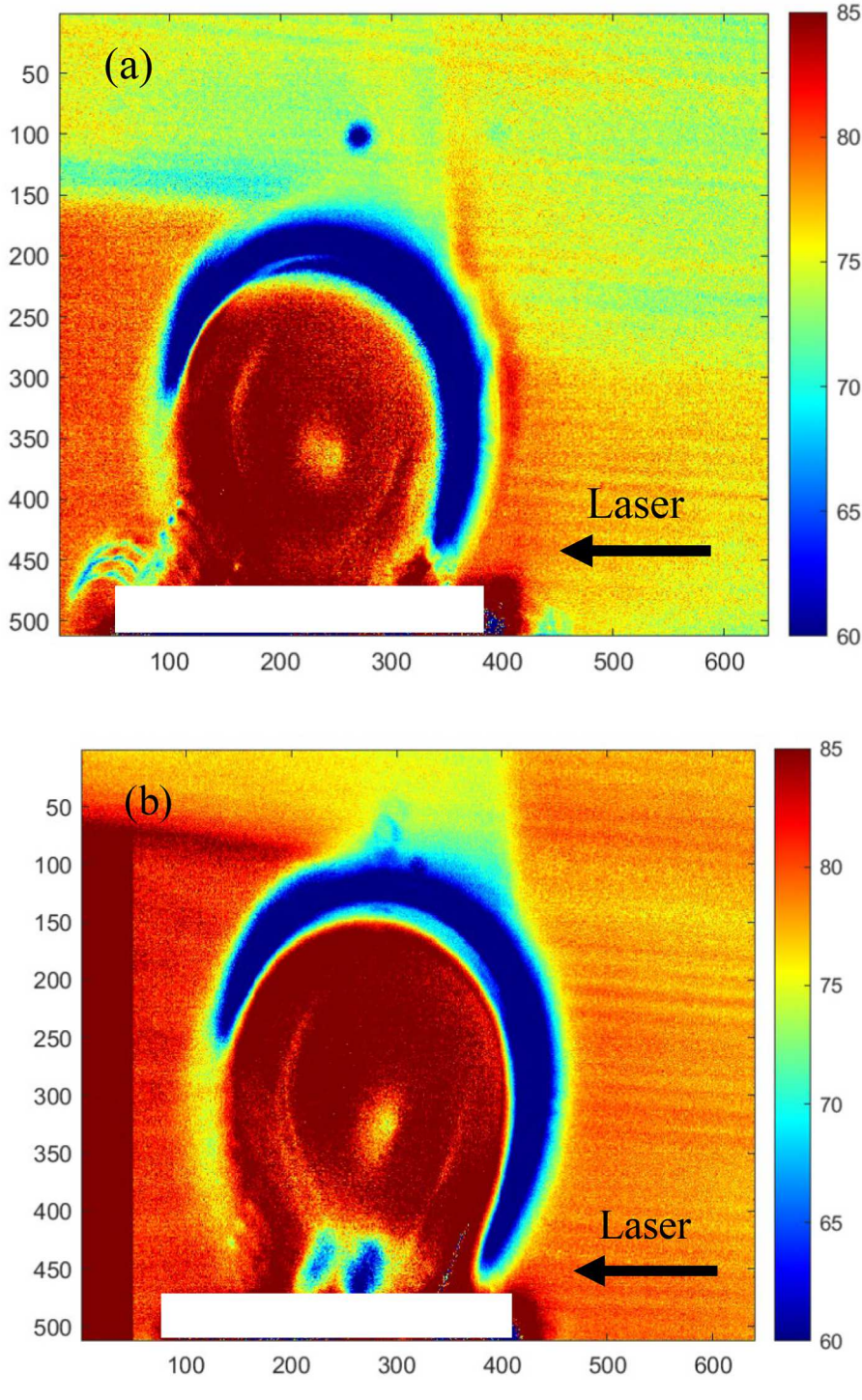


Fig. 13. Liquid temperature distributions near a bubble during growth at approximately a) 8 s, and b) 10 s after initiation on a 0° surface.

bubble initiation on 30° surface. The temperature profile at y_3 shows a sharp increase near the liquid-vapor interface and the heated surface, indicating significant heat transfer from the heated surface ($T_{\rm surface}=110~^\circ\text{C}$) to the surrounding liquid ($T_{y_3=0}=91.3^\circ\text{C}$). These results are consistent with the expected behavior of convective heat transfer in the vicinity of the surface. The temperature gradients at y_1 , y_2 , and y_3 locations over a 0.4 mm distance ($\Delta T/\Delta x$) are approximately 2.5 1.6, and 9.1 °C, respectively, suggesting that the heat transfer rate is highest at y_3 and decreases at y_2 and y_3 . Furthermore, the liquid temperature at the three y locations approaches the bulk liquid temperature ($T=75~^\circ\text{C}$) along the distance, which is consistent with the conduction heat transfer

in liquid away from the bubble, in which convection effects are relatively weak compared to diffusion (conduction) effects [25]. This typically happens when the flow velocity is low.

One interesting observation is that the average liquid temperature at y_1 ($T \approx 84.5$ °C) is higher than that at y_2 ($T \approx 83.3$ °C), despite y_2 being positioned closer to the heated surface. This seemingly contradictory phenomenon is attributed to the occurrence of upward hot liquid movements during bubble growth, which has been captured and studied using DFT along with high-speed imaging techniques. The hot liquid is similar to a rising band and flames of intense heat moving towards the liquid surface (Fig. 17a). This band showcases varying thicknesses,

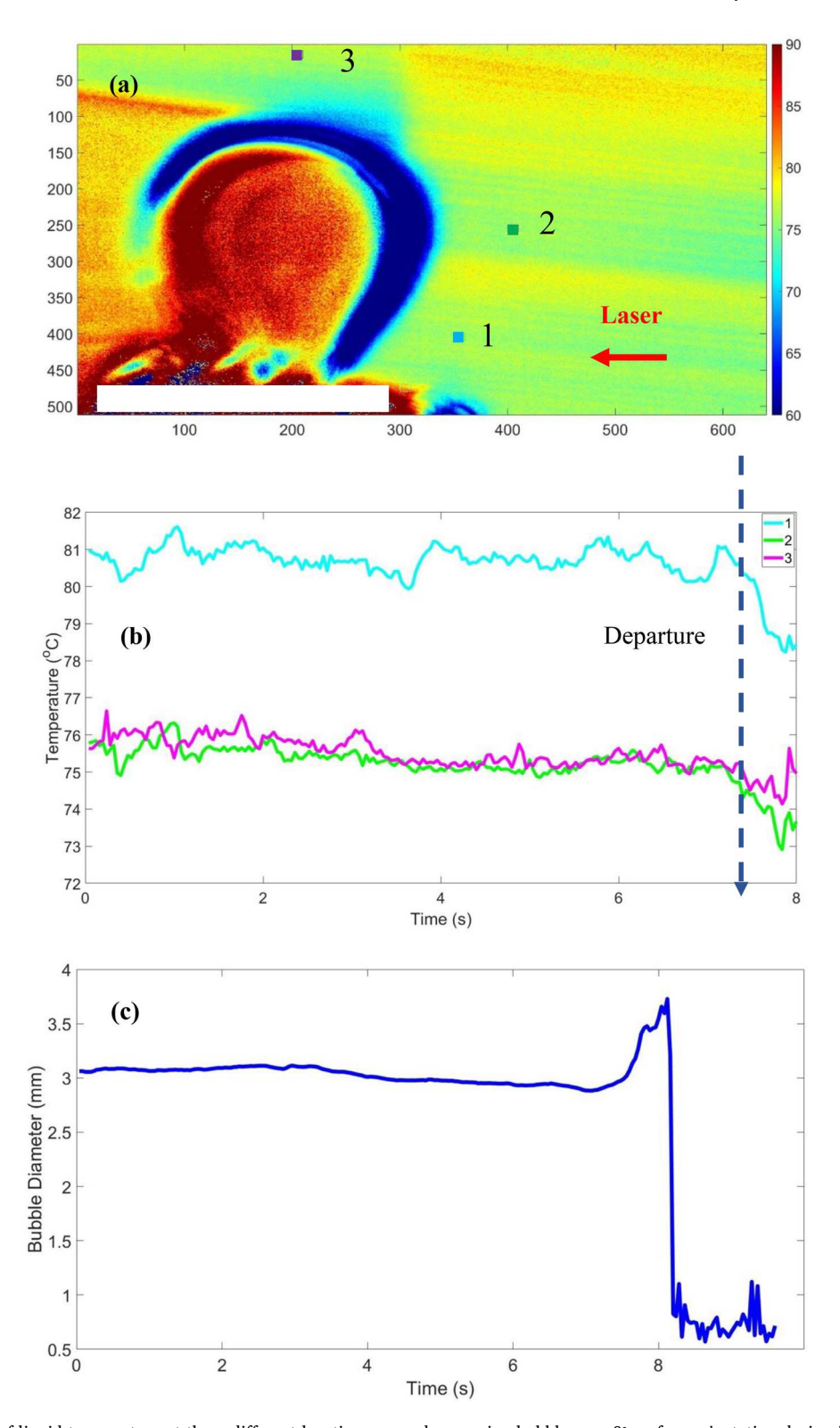


Fig. 14. a) A distribution of liquid temperature at three different locations around a growing bubble on a 0° surface orientation during its departure, b) transient temperature profiles, including the bubble expansion and shrinkage, and c) a bubble diameter over time.

ranging from $\delta=100-500\mu m$. To visualize the impact of this heated band, refer to Fig. 17d, where its influence is clearly depicted at x_1 and x_2 . Examining Fig. 17b and 17d, we observe $\Delta T \approx 4$ °C temperature fluctuations occurring every 100–150 μm along x_1 and x_2 , manifesting as alternating upward and downward shifts. The reason is that the hot liquid undergoes thermal convection, where a heated portion of the liquid rise towards the cooler surface due to density differences. This

convection process creates the ascending band of intense heat.

In Fig. 18a and 18b, two consecutive images during boiling around a single bubble vividly illustrate the rising bands and flames. These images capture the dynamic progression of the phenomenon over time. The hot liquid resembles a rising band and flames of intense heat, akin to those depicted in Fig. 17a, steadily moving towards the liquid surface. This band exhibits varying thicknesses, spanning from $\delta{=}100{-}500~\mu{m}$, as

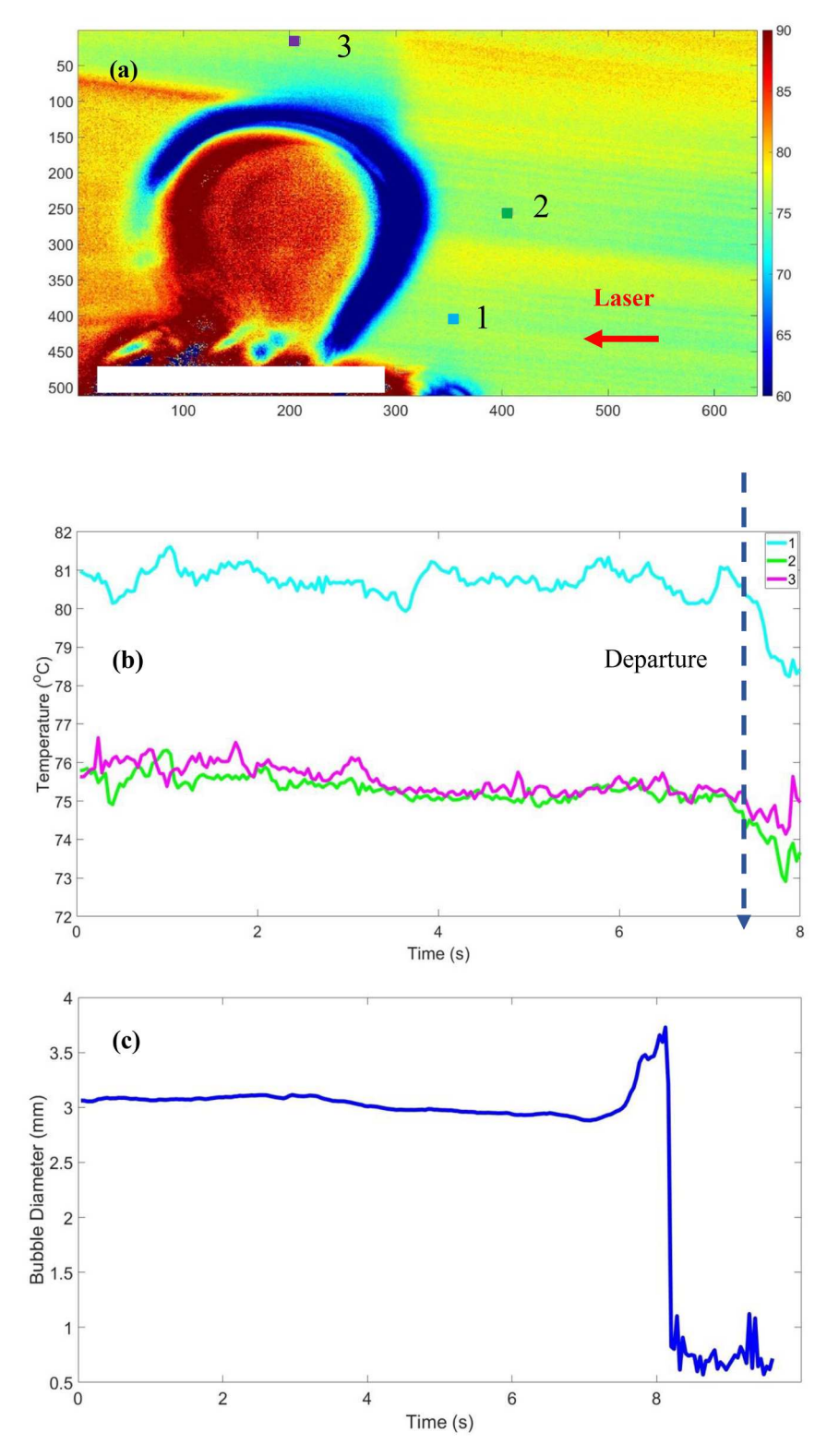


Fig. 15. a) A distribution of liquid temperature at three different locations around a growing bubble on a 30° surface orientation during its departure, b) transient temperature profiles, and c) a bubble diameter over time.

showcased in Fig. 17d, where its influence at x_1 and x_2 is clearly depicted. The consecutive depiction in Figs. 18a and 18b offers a detailed insight into the evolving dynamics of the boiling process and the propagation of heat within the liquid (see the video in the Supplementary Materials).

Fig. 19 the temperature profiles along y_1 , y_2 , and y_3 at t = 8 s after the bubble initiation on 90° surface. Fig. 19b further supports the existence

of hot liquid band moving upward (the average liquid temperature at $y_1(T_{avg,y1}=89.2^{\circ}C)$ is higher than that at $y_3(T_{avg,y3}=87.8^{\circ}C)$.

3.5. Effect of surface orientation on heat transfer coefficient and heat flux

The DFT-based temperature measurements are employed to estimate

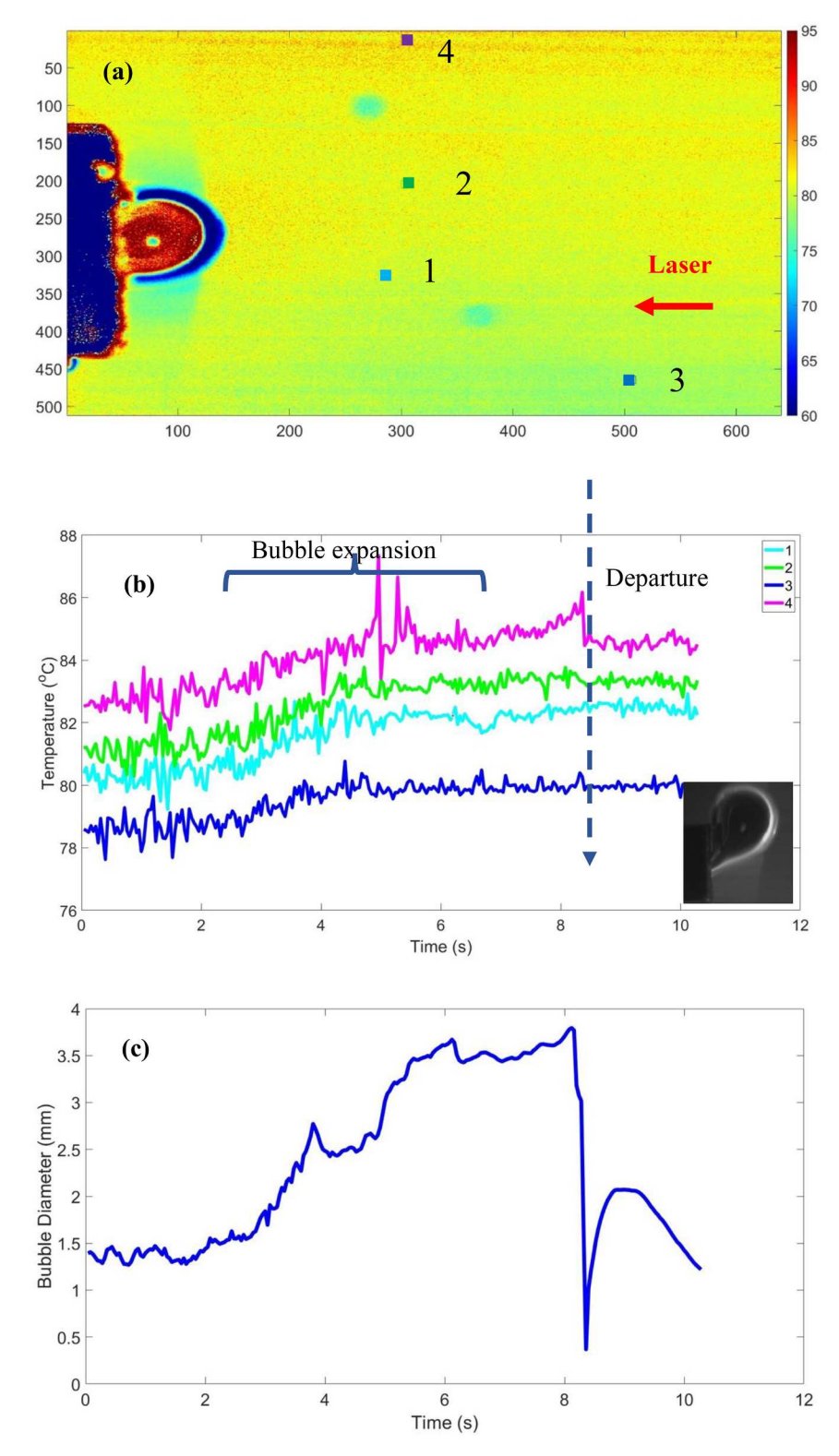


Fig. 16. a) A distribution of liquid temperature at three different locations around a growing bubble on a 90° surface orientation during its departure, b) transient temperature profiles, and c) a bubble diameter over time.

heat transfer coefficients associated with bubble growth, considering the 90° surface as a representative surface orientation. To ensure precise estimations of heat transfer coefficients, we utilize the Rohsenow empirical correlation (Eq. (4)), which has shown excellent agreement with experimental measurements. In this correlation, the heat transfer coefficient (h) is estimated using physical properties of the liquid, including density ρ_l , specific heat (c), latent heat of vaporization (h_{fg}),

and the diameter of the bubble (d) formed during boiling. Additionally, the correlation includes a dimensionless parameter, q, that characterizes the heat flux and a power exponent, m, that depends on the mode of boiling [26–28].

$$h = B \cdot \rho_l^{0.5} c_l^{0.5} \left(h_{fg} d \right)^{0.25} \cdot q^{m+0.5} \cdot \Delta T^{m+0.25}$$
(4)

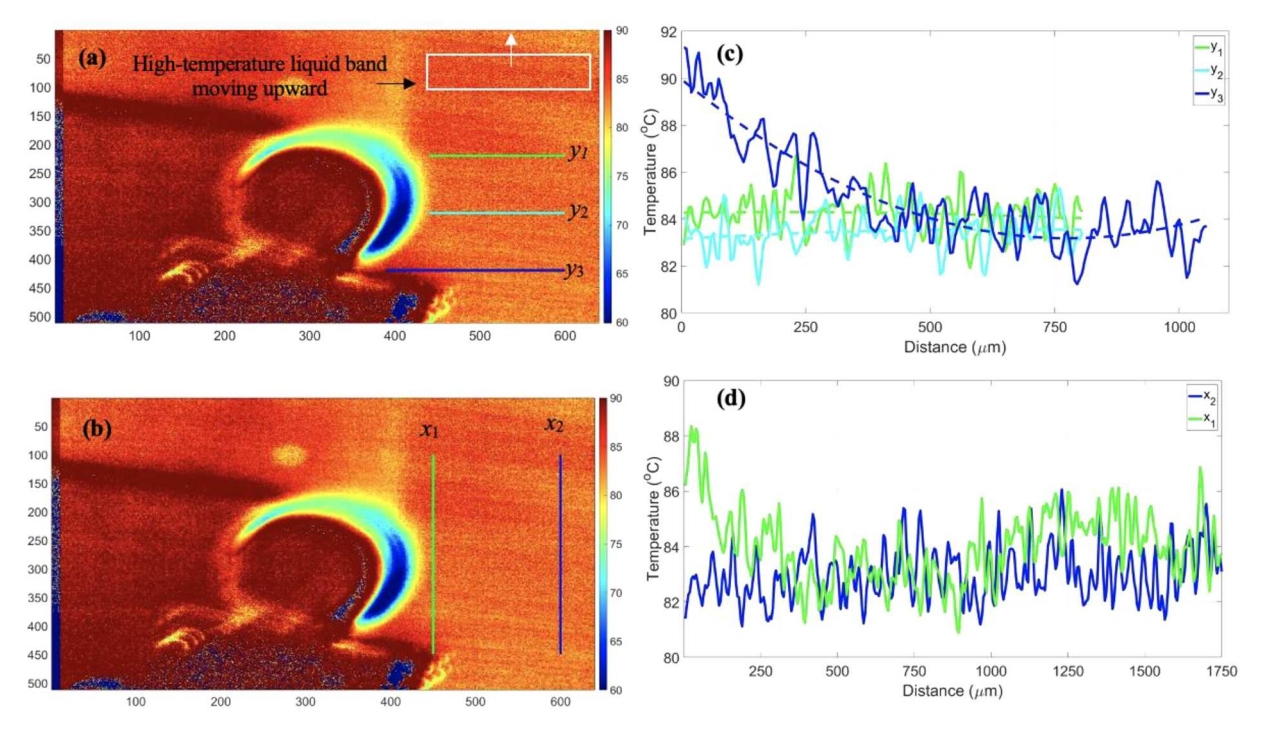


Fig. 17. (a, b) Liquid temperature distributions surrounding a growing bubble at 8 s after initiation on 30° surface. The lines at different x and y locations are shown to measure temperature profiles. (c, d) Temperature profiles along horizontal lines (y_1, y_2, y_3) and vertical lines (x_1, x_2) .

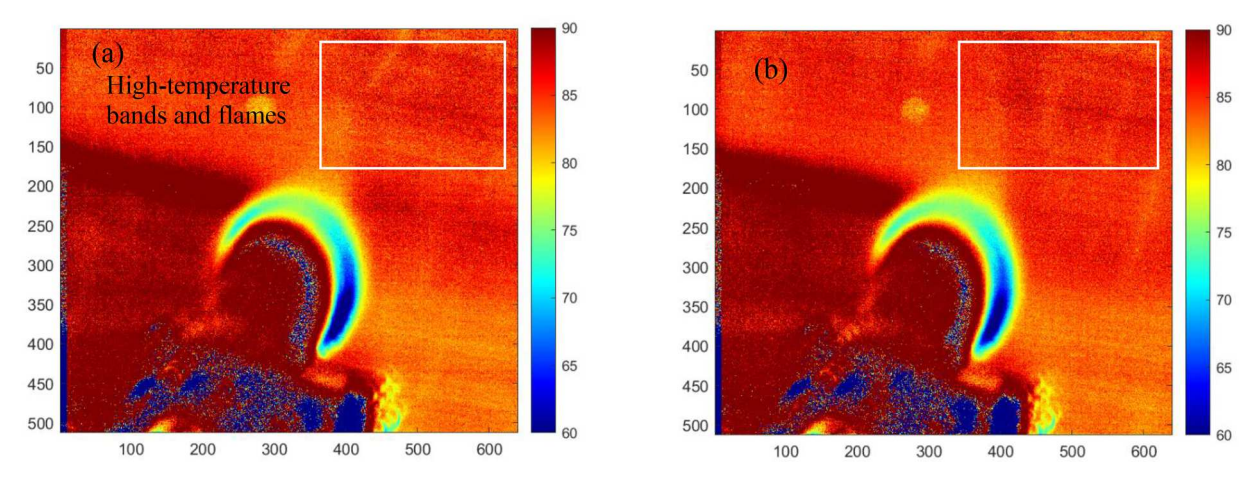


Fig. 18. Two consecutive images of liquid temperature distributions surrounding a growing bubble at 8 s after initiation on 30° surface (a) first and (b) second.

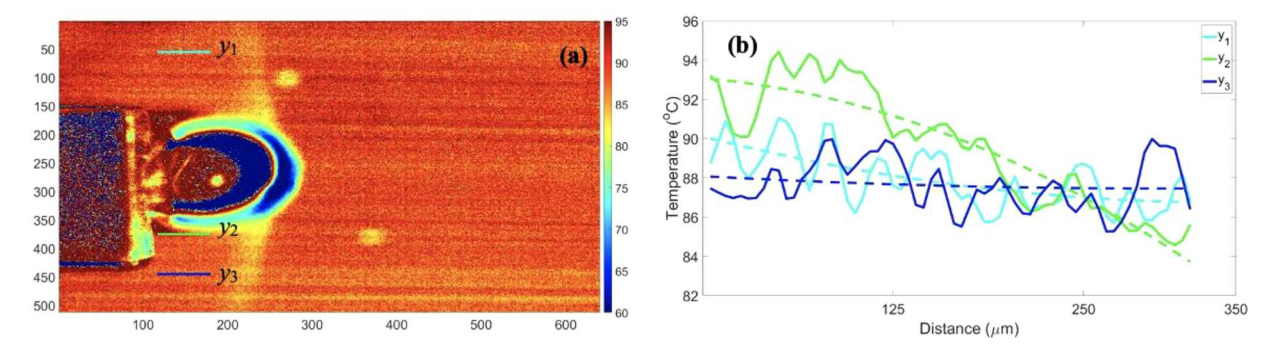


Fig. 19. a) Liquid temperature distributions surrounding a growing bubble at 8 s after initiation on 90° surface. The lines at different y locations are shown to measure temperature profiles. b) Temperature profiles along horizontal lines (y_1, y_2, y_3) .

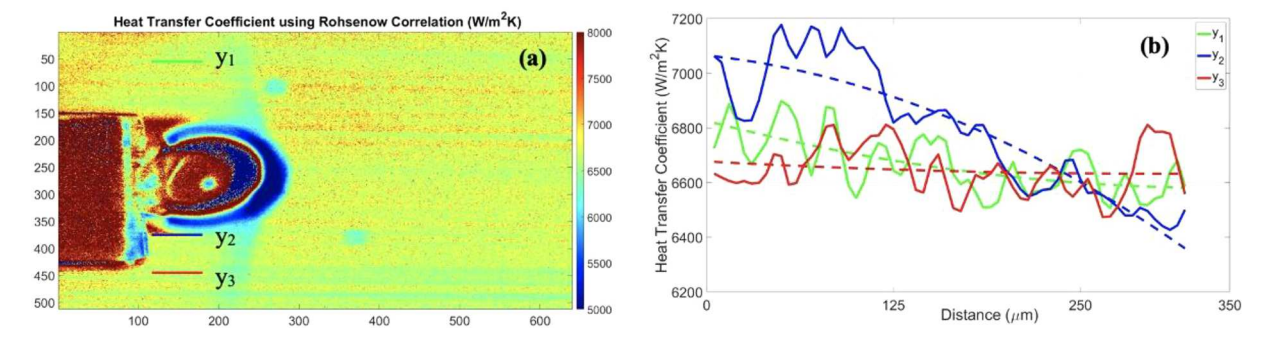


Fig. 20. a) A distribution of heat transfer coefficients estimated by the Rohsenow correlation and b) a variation of heat transfer coefficients on horizontal lines at t = 8 s after the bubble initiation on a 90° surface orientation.

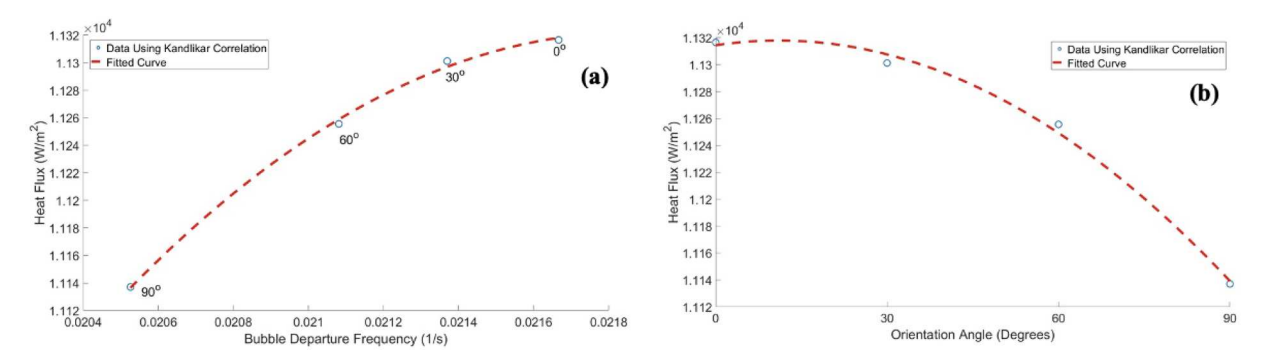


Fig. 21. Heat flux estimated by the Kandlikar correlation [29] a) based on experimental data for the bubble departure frequency and b) corresponding surface orientation

In addition, we utilize the correlation proposed by Kandlikar et al. [29] to estimate heat flux based on the bubble departure diameter, bubble departure frequency, active nucleation site density, and thermal-physical properties of liquid. The expression of the heat flux during discrete bubble region is

$$q' = \frac{C^2}{2} \sqrt{\pi (k\rho c_p) f_b} D_b^2 N_a' \Delta T$$
 (5)

where C, f_b , D_b , N_a^r represent a constant for bubble area influence, the bubble departure frequency, bubble departure diameter, and active nucleation site density, respectively. ΔT is the wall superheat.

Fig. 20a and 20b show a distribution of heat transfer coefficients around the bubble on the 90° surface orientation and profiles of heat transfer coefficients along selected horizontal lines, estimated by the Rohsenow correlation. These figures show that heat transfer coefficients are higher close to the liquid-vapor interface, heated surface, and in the superheated liquid layer than that in the bulk liquid. The estimated Δh values for the three horizontal lines y_1 , y_2 , and y_3 are 250 W/m²·K, 503 W/m²·K, and 76 W/m²·K, respectively, for a 0.25 mm on the lines. These values indicate a substantial variation in heat transfer coefficients along the horizontal lines, reflecting the spatial distribution of heat transfer around the bubble. In Fig. 20b (blue line), we observe that the heat transfer coefficient is higher in proximity to the liquid-vapor interface and the heated surface ($\approx 7100 \text{ W/m}^2\text{K}$) compared with the bulk liquid $(\approx 6500 \text{ W/m}^2\text{K})$. This observation aligns with our understanding that the heated surface and the thermal layer play a crucial role in heat transfer during bubble growth. Fig. 21a and 21b show heat flux estimated by the Kandlikar correlation [29] based on experimental data for the bubble departure frequency and its corresponding surface orientation. According to Fig. 21, heat flux increases from 1.114×10^4 W/m² for 90° to 1.132×10^{4} W/m² for 0° surface orientations due to the increased bubble departure frequency.

4. Conclusion

In this study, the dual tracer laser-induced fluorescence thermometry technique (DFT) was employed with thin film illumination to measure 2D bulk fluid temperature fields near the growing bubble on different surface orientations within 0.3 $^{\circ}\text{C}$ at a 30 μm resolution. Multiple 2D temperature fields have been, on different layers, utilized to recontruct 3D temperature fields near the growing bubble. The study's noteworthy findings are summarized below:

- Increasing the surface orientation results in a larger bubble base diameter due to the buoyancy force, which leads to a lower bubble departure frequency (the bubble tends to attach to the surface longer). This behavior is particularly evident at low heat flux levels when there are no neighboring bubbles merging, and the heated surface area is limited.
- A progressive increase in average liquid temperature can be seen as the surface orientation approaches perpendicular (90°). This phenomenon can be explained by the combined effects of liquid replenishment and the convective heat transfer associated with the bubble motion (bubble departure frequency).
- At a surface orientation of 0° (horizontal surface), the bubble tends to detach relatively quickly. As a result, the liquid surrounding the bubble is exposed to the heated surface for a shorter period, limiting the time available for heat transfer. Therefore, the temperature rise in the liquid is relatively smaller compared to higher surface orientations.

This study provides valuable insights into local temperature distributions surrounding a growing bubble during nucleate boiling, which can aid in optimizing the thermal management of extreme heat loads in electrical systems. The study's findings highlight the highly transient of the temperature distribution around a single bubble, emphasizing the need to accurately measure and account for these dynamics in thermal

transport models.

CRediT authorship contribution statement

Mahyar Ghazvini: Writing – review & editing, Writing – original draft, Software, Methodology, Investigation, Formal analysis, Data curation, Conceptualization. Mazen Hafez: Writing – review & editing, Validation, Methodology, Data curation, Conceptualization. Cristian Pena: Writing – review & editing, Methodology, Investigation, Formal analysis, Data curation. Philippe Mandin: Writing – review & editing, Investigation, Conceptualization. Rosalinda Inguanta: Writing – review & editing, Investigation, Conceptualization. Myeongsub Kim: Conceptualization, Methodology, Supervision, Writing – original draft, Writing – review & editing.

Declaration of competing interest

The authors declare the following financial interests/personal relationships which may be considered as potential competing interests:

Myeongsub Kim reports financial support was provided by National Science Foundation. If there are other authors, they declare that they have no known competing financial interests or personal relationships that could have appeared to influence the work reported in this paper.

Data availability

Data will be made available on request.

Supplementary materials

Supplementary material associated with this article can be found, in the online version, at doi:10.1016/j.ijheatmasstransfer.2024.125517.

References

- [1] K.N. Rainey, S.M. You, Effects of heater size and orientation on pool boiling heat transfer from microporous coated surfaces, Int. J. Heat Mass Transf. 44 (2001) 2589–2599, https://doi.org/10.1016/S0017-9310(00)00318-5.
- [2] B.D. Marcus, D. Dropkin, The effect of surface configuration on nucleate boiling heat transfer, Int. J. Heat Mass Transf. 6 (1963) 863–866, https://doi.org/ 10.1016/0017-9310(63)90069-3
- [3] P.M. Githinji, R.H. Sabersky, Some effects of the orientation of the heating surface in nucleate boiling, J. Heat Transfer. 85 (1963) 379, https://doi.org/10.1115/ 1.3686129, -379.
- [4] Y. Mei, Y. Shao, S. Gong, Y. Zhu, H. Gu, Effects of surface orientation and heater material on heat transfer coefficient and critical heat flux of nucleate boiling, Int. J. Heat Mass Transf. 121 (2018) 632–640, https://doi.org/10.1016/J. LJHEATMASSTRANSFER.2018.01.020.
- [5] M.S. El-Genk, A. Suszko, Effects of inclination angle and liquid subcooling on nucleate boiling on dimpled copper surfaces, Int. J. Heat Mass Transf. 95 (2016) 650–661, https://doi.org/10.1016/J.IJHEATMASSTRANSFER.2015.12.048.
- [6] A. Priarone, Effect of surface orientation on nucleate boiling and critical heat flux of dielectric fluids, Int. J. Therm. Sci. 44 (2005) 822–831, https://doi.org/ 10.1016/J.IJTHERMALSCI.2005.02.014.
- N. Kaneyasu, F. Yasunobu, U. Satoru, O. Haruhiko, Effect of surface configuration on nucleate boiling heat transfer, Int. J. Heat Mass Transf. 27 (1984) 1559–1571, https://doi.org/10.1016/0017-9310(84)90268-0.
- [8] M. Kim, M. Yoda, Dual-tracer fluorescence thermometry measurements in a heated channel, Exp. Fluids 491 (49) (2010) 257–266, https://doi.org/10.1007/S00348-010-0853-9, 2010.

- [9] J. Sakakibara, R.J. Adrian, Measurement of temperature field of a Rayleigh-Bénard convection using two-color laser-induced fluorescence, Exp. Fluids 373 (37) (2004) 331–340, https://doi.org/10.1007/S00348-004-0821-3, 2004.
- [10] M. Kim, M. Yoda, The spatial resolution of dual-tracer fluorescence thermometry in volumetrically illuminated channels, Exp. Fluids. 55 (2014) 1–12, https://doi.org/ 10.1007/S00348-013-1649-5/METRICS.
- [11] J.P. Crimaldi, The effect of photobleaching and velocity fluctuations on single-point LIF measurements, Exp. Fluids 234 (23) (1997) 325–330, https://doi.org/10.1007/S003480050117, 1997.
- [12] G.W. Walker, V.C. Sundar, C.M. Rudzinski, A.W. Wun, M.G. Bawendi, D.G. Nocera, Quantum-dot optical temperature probes, Appl. Phys. Lett. 83 (2003) 3555, https://doi.org/10.1063/1.1620686.
- [13] J. Coppeta, C. Rogers, Dual emission laser induced fluorescence for direct planar scalar behavior measurements, Exp. Fluids. 25 (1998) 1–15, https://doi.org/ 10.1007/S003480050202/METRICS.
- [14] M. Tange, K. Kuribayashi, A. Abdelghany, Temperature measurement around multiple boiling bubbles in a confined space using two-color laser-induced fluorescence, J. Therm. Sci. Technol. 16 (2021) 1–9, https://doi.org/10.1299/ ITST 2021 ITST 2021.
- [15] A. Abdelghany, K. Kuribayashi, M. Tange, Ratiometric laser-induced fluorescence for liquid-phase thermometry around boiling bubbles at extended temperatures above 70°C, Exp. Fluids. 63 (2022) 1–9, https://doi.org/10.1007/S00348-022-03397-7/METRICS.
- [16] M. Ghazivini, M. Hafez, A. Ratanpara, M. Kim, A review on correlations of bubble growth mechanisms and bubble dynamics parameters in nucleate boiling, J. Therm. Anal. Calorim. 2021. (2021) 1–37, https://doi.org/10.1007/S10973-021-10876-2.
- [17] M. Takeyama, M. Zupančič, T. Kunugi, Influence of hydrodynamic interactions among multiple bubbles on convective heat transfer in nucleate boiling, Exp. Therm. Fluid Sci. 128 (2021) 110449, https://doi.org/10.1016/J. EXPTHERMFLUSCI.2021.110449.
- [18] M. Takeyama, T. Kunugi, Flow behavior around single nucleate boiling bubble quantitatively grasped by particle tracking visualization, Int. J. Multiph. Flow. 129 (2020) 103295, https://doi.org/10.1016/J.IJMULTIPHASEFLOW.2020.103295.
- [19] J. Coppeta, C. Rogers, Dual emission laser induced fluorescence for direct planar scalar behavior measurements, Exp. Fluids 251 (25) (1998) 1–15, https://doi.org/ 10.1007/S003480050202, 1998.
- [20] M.B. Shafii, C.L. Lum, M.M. Koochesfahani, In situ LIF temperature measurements in aqueous ammonium chloride solution during uni-directional solidification, Exp. Fluids 484 (48) (2009) 651–662, https://doi.org/10.1007/S00348-009-0758-7, 2009.
- [21] M.H. Ghazvini, P.Mandin Mahyar, M. Kim, Experimental study of pool boiling heat transfer on novel fin surfaces, Int. J. Multiph. Flow. (2023).
- [22] L. Favre, C. Colin, S. Pujet, S. Mimouni, An updated force balance approach to investigate bubble sliding in vertical flow boiling at low and high pressures, Int. J. Heat Mass Transf. 211 (2023) 124227, https://doi.org/10.1016/J. IJHEATMASSTRANSFER.2023.124227.
- [23] J.M. Kim, J.H. Kim, H.S. Ahn, Hydrodynamics of nucleate boiling on downward surface with various orientation. Part I: departure diameter, frequency, and escape speed of the slug, Int. J. Heat Mass Transf. 116 (2018) 1341–1351, https://doi.org/ 10.1016/J.IJHEATMASSTRANSFER.2017.07.041.
- [24] H. Choi, F. Aziz, Y. Shin, W. Hwang, K.Y. Lee, D. Jo, Effects of super-hydrophilicity and orientation of heater surface on bubble behavior and the critical heat flux in pool boiling, Ann. Nucl. Energy. 186 (2023) 109762, https://doi.org/10.1016/J. ANUCENE.2023.109762.
- [25] W. Gao, J. Qi, X. Yang, J. Zhang, D. Wu, Experimental investigation on bubble departure diameter in pool boiling under sub-atmospheric pressure, Int. J. Heat Mass Transf. 134 (2019) 933–947, https://doi.org/10.1016/j. ijheatmasstransfer.2019.01.024.
- [26] M.R. Mohaghegh, A. Raihan, M. Siddique, S. Mahmud, S. Tasnim, A new correlation for the onset of nucleate boiling heat flux under an impinging planar water jet, (2020). 10.11159/ffhmt20.174.
- [27] D.S. Wen, B.X. Wang, Effects of surface wettability on nucleate pool boiling heat transfer for surfactant solutions, Int. J. Heat Mass Transf. 45 (2002) 1739–1747, https://doi.org/10.1016/S0017-9310(01)00251-4.
- [28] I. Nejati, A. Sielaff, B. Franz, M. Zimmermann, P. Hänichen, K. Schweikert, J. Krempel, P. Stephan, A. Martin, H. Scheerer, T. Engler, M. Oechsner, Experimental investigation of single bubble nucleate bolling in microgravity, Microgravity Sci. Technol. 32 (2020) 597–607, https://doi.org/10.1007/S12217-020-09813-Z/METRICS.
- [29] S.G. Kandlikar, Handbook of phase change: boiling and condensation, Handb. Phase Chang. Boil. Condens. (2019), https://doi.org/10.1201/9780203752654/ HANDBOOK-PHASE-CHANGE-KANDLIKAR.